Inorg. Chem. **2008**, *47*, 2975−2986

Inorganic Chemistry
Article

Structural Model Studies for the Peroxo Intermediate P and the Reaction Pathway from P → Q of Methane Monooxygenase Using Broken-Symmetry Density Functional Calculations

Wen-Ge Han and Louis Noodleman*

Department of Molecular Biology, TPC15, The Scripps Research Institute, 10550 North Torrey Pines Road, La Jolla, California 92037

Received June 18, 2007

Several structural models for the active site of the peroxo intermediate state “P” of the hydroxylase component of soluble methane monooxygenase (MMOH) have been studied, using two DFT functionals OPBE and PW91 with broken-symmetry methodology and the conductor-like screening (COSMO) solvation model. These active site models have different O_2 binding modes to the diiron center, such as the μ-η^2,η^2, *trans*-μ−1,2 and *cis*-μ−1,2 conformations. The calculated properties, including optimized geometries, electronic energies, Fe net spin populations, and Mössbauer isomer shift and quadrupole splitting values, have been reported and compared with available experimental results. The high-spin antiferromagnetically (AF) coupled Fe^{3+} sites are correctly predicted by both OPBE and PW91 methods for all active site models. Our data analysis and comparisons favor a *cis*-μ−1,2 structure (model *cis*-μ−1,2a shown in Figure 9) likely to represent the active site of MMOH-P. Feasible structural changes from MMOH-P to another intermediate state MMOH-Q are also proposed, where the carboxylate group of Glu243 side chain has to open up from the mono-oxygen bridging position, and the dissociations of the terminal H_2O ligand from Fe1 and of the oxygen atom in the carboxylate group of Glu144 from Fe2 are also necessary for the O_2 binding mode changes from cis to trans. The O−O bond is proposed to break in the trans-conformation and forms two μ-oxo bridges in MMOH-Q. The terminal H_2O molecule and the Glu144 side chain then rebind with Fe1 and Fe2, respectively, in Q.

1. Introduction

Soluble methane monooxygenase (MMO) found in methanotrophic bacteria catalyzes the hydroxylation of methane, which requires cleavage of stable and nonpolar C−H bond in methane (converting methane to methanol).[1–3] The MMO enzyme consists of at least three components: a hydroxylase protein (MMOH); a regulatory protein for molecular oxygen binding, called component B (MMOB); and a reductase (MMOR), which comprises three distinct domains—[2Fe2S] ferredoxin and FAD- and NADH-binding domains— and provides two electrons to the hydroxylase.[4] A fourth component, MMOD, whose function is still not known, has recently been characterized and found to bind to MMOH. It is a potent inhibitor of MMO.[5,6] MMOH contains a carboxylate-bridged nonheme diiron center at its active site and catalyzes the transformation of methane plus oxygen to methanol and water. The reaction cycle of MMOH with methane or other alkanes can be summarized by the following set of reactions

$$Fe^{3+}(OH^-)_2Fe^{3+} + 2e^- + 2H^+ \rightarrow 2Fe^{2+} + 2H_2O \quad (I)$$

$$2Fe^{2+} + O_2 \rightarrow \text{Intermediate-P}\{Fe^{3+}(O-O)Fe^{3+}\} \rightarrow \text{Intermediate-Q}\{Fe^{4+}(\mu\text{-}O)_2Fe^{4+}\} \quad (II)$$

---

* To whom correspondence should be addressed. E-mail: lou@scripps.edu. Fax: 858-7848896.

(1) Wallar, B. J.; Lipscomb, J. D. *Chem. Rev.* **1996**, *96*, 2625–2657.
(2) Solomon, E. I.; Brunold, T. C.; Davis, M. I.; Kemsley, J. N.; Lee, S. K.; Lehnert, N.; Neese, F.; Skulan, A. J.; Yang, Y. S.; Zhou, J. *Chem. Rev.* **2000**, *100*, 235–349.
(3) Jin, Y.; Lipscomb, J. D. *J. Biol. Inorg. Chem.* **2001**, *6*, 717–725.
(4) Chatwood, L. L.; Muller, J.; Gross, J. D.; Wagner, G.; Lippard, S. J. *Biochemistry* **2004**, *43*, 11983–11991.
(5) Merkx, M.; Lippard, S. J. *J. Biol. Chem.* **2002**, *277*, 5858–5865.
(6) Rinaldo, D.; Philipp, D. M.; Lippard, S. J.; Friesner, R. A. *J. Am. Chem. Soc.* **2007**, *129*, 3135–3147.

10.1021/ic701194b CCC: $40.75

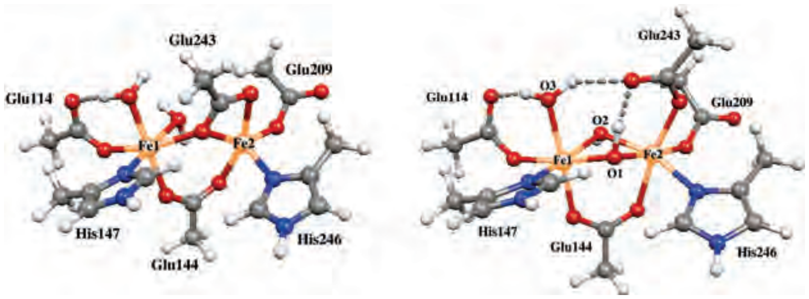

Figure 1. Reduced diferrous (left) and oxidized diferric (right) active site structures of MMOH.

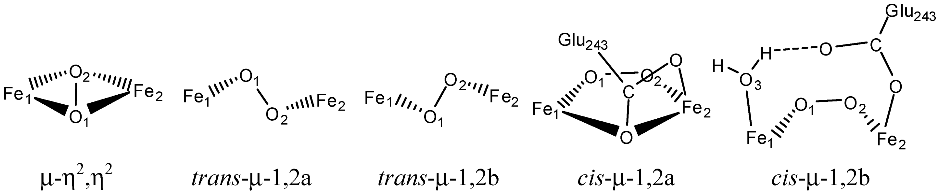

μ-η^2,η^2 *trans*-μ-1,2a *trans*-μ-1,2b *cis*-μ-1,2a *cis*-μ-1,2b

Figure 2. Possible O_2 binding conformations in the MMOH-peroxo intermediate P. Calculations of these active site models are presented in the current paper.

$$\text{Intermediate-Q}\{Fe^{4+}\ (\mu\text{-}O)_2Fe^{4+}\} + R-H + H_2O \rightarrow Fe^{3+}(OH^-)_2Fe^{3+} + R-OH \quad \text{(III)}$$

where R = methane or the higher alkanes. This simple sequence of reaction steps belies the structural and energetic complexities associated with the catalytic process. Coupled electron and proton addition to the $Fe^{3+}Fe^{3+}$ resting enzyme generates the reduced $Fe^{2+}Fe^{2+}$ state. The reduced complex is then oxidized by a direct reaction with an oxygen molecule. Several intermediates in this reaction have been observed. Two of them are spectroscopically and kinetically characterized and are named P and Q.[7–12] Despite the collective experimental effort, structures of these intermediate species are not yet available. Based on Mössbauer[8] and resonance Raman spectroscopy studies, P has been suggested to be an Fe^{3+} (O−O)Fe^{3+} peroxo complex. The Mössbauer spectrum of P species in *Methylococcus capsulatus* (Mc) (Bath) system is a sharp symmetric quadrupole doublet with isomer shifts (δ) and quadrupole splittings (ΔE_Q) of ($\delta = 0.66$ mm s^{-1}, $\Delta E_Q = 1.51$ mm s^{-1}),[8] which indicates that O_2 binds with Fe1 and Fe2 in a symmetric way. The peroxo intermediate subsequently converts to intermediate Q, which is the species that reacts with methane to form methanol, and is proposed to have two near-equivalent high-spin Fe^{4+} sites that are antiferromagnetically (AF) coupled.[8,9] The Mössbauer spectra of Q in both Mc (Bath) and *Methylosinus trichosporium* (Mt) OB3b systems were also reported.[8,9] These spectroscopic parameters of the intermediates were obtained with MMOB present.

Several active site structural models of P and Q have been studied theoretically by different groups.[6,13–28] Models were established based on the active sites (see Figure 1) of the reduced diferrous and oxidized diferric X-ray crystal structures of MMOH without MMOB present.[29,30] Possible peroxo O−O binding structures of P are shown in Figure 2.

A recent QM/MM study by Friesner and Lippard's group favors the μ-η^2,η^2 structure for intermediate P because it is more stable than other model structures they studied.[6] On the basis of the vibrational spectra calculations, Yoshizawa[13,14,16] and Solomon's[17] groups proposed that the *cis*-μ−1,2 mode is the most favorable one for binding of O_2 to the diiron center of MMOH.

---

(7) Lee, S. K.; Nesheim, J. C.; Lipscomb, J. D. *J. Biol. Chem.* **1993**, *268*, 21569–21577.

(8) Liu, K. E.; Valentine, A. M.; Wang, D. L.; Huynh, B. H.; Edmondson, D. E.; Salifoglou, A.; Lippard, S. J. *J. Am. Chem. Soc.* **1995**, *117*, 10174–10185.

(9) Lee, S. K.; Fox, B. G.; Froland, W. A.; Lipscomb, J. D.; Münck, E. *J. Am. Chem. Soc.* **1993**, *115*, 6450–6451.

(10) Shu, L. J.; Nesheim, J. C.; Kauffmann, K.; Munck, E.; Lipscomb, J. D.; Que, L. *Science* **1997**, *275*, 515–518.

(11) Beauvais, L. G.; Lippard, S. J. *J. Am. Chem. Soc.* **2005**, *127*, 7370–7378.

(12) Beauvais, L. G.; Lippard, S. J. *Biochem. Biophys. Res. Commun.* **2005**, *338*, 262–266.

(13) Yoshizawa, K.; Hoffmann, R. *Inorg. Chem.* **1996**, *35*, 2409–2410.

(14) Yoshizawa, K.; Yokomichi, Y.; Shiota, Y.; Ohta, T.; Yamabe, T. *Chem. Lett.* **1997**, 587–588.

(15) Yoshizawa, K. *J. Inorg. Biochem.* **2000**, *78*, 23–34.

(16) Yumura, T.; Yoshizawa, K. *Bull. Chem. Soc. Jpn.* **2004**, *77*, 1305–1311.

(17) Brunold, T. C.; Tamura, N.; Kitajima, N.; Moro-oka, Y.; Solomon, E. I. *J. Am. Chem. Soc.* **1998**, *120*, 5674–5690.

(18) Musaev, D. G.; Basch, H.; Morokuma, K. *J. Am. Chem. Soc.* **2002**, *124*, 4135–4148.

(19) Siegbahn, P. E. M.; Crabtree, R. H. *J. Am. Chem. Soc.* **1997**, *119*, 3103–3113.

(20) Siegbahn, P. E. M. *Inorg. Chem.* **1999**, *38*, 2880–2889.

(21) Siegbahn, P. E. M.; Blomberg, M. R. A. *Annu. Rev. Phys. Chem.* **1999**, *50*, 221–249.

(22) Siegbahn, P. E. M. *J. Biol. Inorg. Chem.* **2001**, *6*, 27–45.

(23) Siegbahn, E. M. *Q. Rev. Biophys.* **2003**, *36*, 91–145.

(24) Dunietz, B. D.; Beachy, M. D.; Cao, Y. X.; Whittington, D. A.; Lippard, S. J.; Friesner, R. A. *J. Am. Chem. Soc.* **2000**, *122*, 2828–2839.

(25) Gherman, B. F.; Dunietz, B. D.; Whittington, D. A.; Lippard, S. J.; Friesner, R. A. *J. Am. Chem. Soc.* **2001**, *123*, 3836–3837.

(26) Baik, M. H.; Newcomb, M.; Friesner, R. A.; Lippard, S. J. *Chem. Rev.* **2003**, *103*, 2385–2419.

(27) Lovell, T.; Han, W.-G.; Liu, T.; Noodleman, L. *J. Am. Chem. Soc.* **2002**, *124*, 5890–5894.

(28) Noodleman, L.; Lovell, T.; Han, W.-G.; Li, J.; Himo, F. *Chem. Rev.* **2004**, *104*, 459–508.

(29) Rosenzweig, A. C.; Nordlund, P.; Takahara, P. M.; Frederick, C. A.; Lippard, S. J. *Chem. Biol.* **1995**, *2*, 409–418.

(30) Elango, N.; Radhakrishnan, R.; Froland, W. A.; Wallar, B. J.; Earhart, C. A.; Lipscomb, J. D.; Ohlendorf, D. H. *Protein Sci.* **1997**, *6*, 556–568.

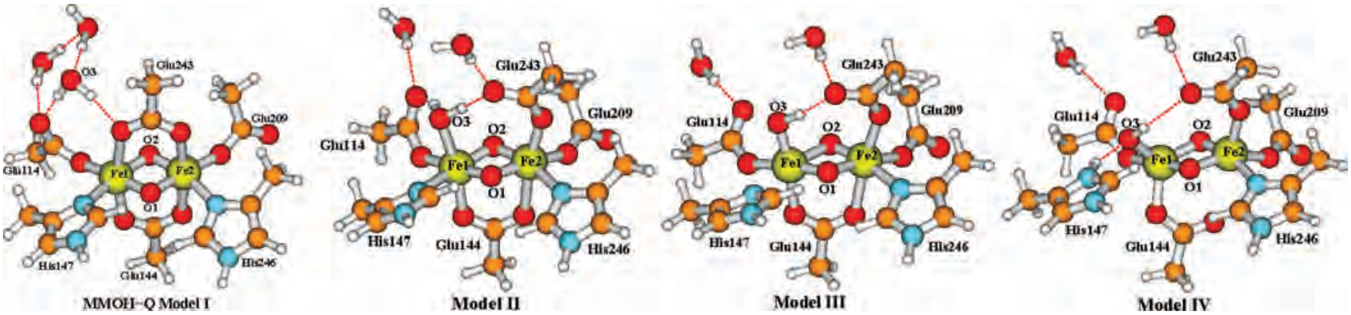

Figure 3. Central diiron structures of our recently studied four MMOH-Q active site models. The second- and third-shell H-bonding residues in these models can be found in Figure 6 of ref 31 and in Figure 4 of current paper.

So far as we know, there are no prior efforts in Mössbauer property calculations on models for intermediate P. In this paper, we will geometry optimize the MMOH-P model clusters indicated in Figure 2 (including second- and third-shell H-bonding residues as well as the first shell metal binding ligands) and identify which peroxo model may represent the active site of intermediate P by comparing their structures, electronic energies, and Mössbauer isomer shift and quadrupole splitting values with available experimental data. After obtaining the favorable P and Q active site structures, it is then possible to propose how O_2 first binds to the diiron centers and how the active site changes from P to Q.

2. Previous Q Calculations—Starting Geometries for P

Very recently,[31] we have studied four active site models (see Figure 3 for the first shell diiron core structures) for MMOH-Q, using DFT functionals OPBE,[32–34] OLYP,[34,35] and PW91,[36] incorporated with broken-symmetry (BS)[37,38] and the conductor-like screening (COSMO)[39–42] solvation model. OPBE is the combination of Handy's optimized exchange (OPTX)[34] and PBE correlation (PBEc) functionals,[32,33] and OLYP is a combination of OPTX and LYP correlation.[35] OPBE and OLYP yield very similar calculated results for our MMOH-Q models.[31]

Model I and II are currently promising active site structures of Q which were proposed by Siegbahn[20,21] and by Friesner and Lippard's group.[25,26] Our detailed calculations and data analysis support model II, which contains an $Fe^{4+}(\mu\text{-}O)_2Fe^{4+}$ center, one axial water which also H-bonds to both side chains of Glu243 and Glu114, and one bidentate carboxylate group from the side chain of Glu144, and is likely to represent the active site of MMOH-Q. Model IV, which has a terminal hydroxo H-bonding to the protonated His147 that is dissociated from the nearby Fe1, has the lowest electronic energy among the four Q models in both OPBE and OLYP calculations.[31] It has been reported that the large value (28 units) of the preedge area for each Fe^{4+} site in Q observed by X-ray absorption experiment implies that the Fe^{4+} centers have a highly distorted geometry and are likely to have coordination number no greater than 5.[10] We therefore thought that our model IV was also a good candidate for intermediate Q because it is more asymmetric in its $Fe(\mu\text{-}O)_2Fe$ diamond core with 5–5 coordination numbers for both Fe sites. However, very recent observations by Que's group were reported that the 6-coordinate high-spin Fe^{3+}-peroxo complexes also show very large values of units in the preedge areas of their X-ray absorption spectra (XAS).[43] This implies that the previous conclusion of the 5 (or lower)-coordinate Fe sites in Q based on the large preedge area of XAS may not be reliable.

On the other hand, all calculated results for MMOH-Q models presented in ref 31 were obtained in COSMO calculations with a dielectric constant $\epsilon = 80.0$. We now extended those calculations (including geometry optimizations and Mössbauer property calculations) for the four MMOH-Q models using both OPBE and PW91 methods in gas-phase and in COSMO solvation model with different dielectric constants of $\epsilon = 4.0$, 10.0 (only for OPBE), and 80.0. The comparison of these properties are given in the Supporting Information (see Tables S1 and S2). The calculated Mössbauer isomer shift and quadrupole splitting values change little with the polarity of the environment. The relative energies among the four models do change with the surrounding dielectric constants. Model IV is not an energy minimum in gas-phase. The proton which transferred to His147 now transferred back to the terminal H_2O during gas-phase geometry optimizations in both OPBE and PW91 methods. Model IV also turns out to be in higher energy than model II in gas-phase and in low dielectric environment of $\epsilon = 4.0$ for OPBE potential, and it is always at higher energy than model II in PW91 calculations. Considering the proton transfer barrier from terminal H_2O to His147 and the energy costs of dissociating His147 from Fe1 with

---

(31) Han, W.-G.; Noodleman, L. *Inorg. Chim. Acta* **2008**, *361*, 973–986.
(32) Perdew, J. P.; Burke, K.; Ernzerhof, M. *Phys. Rev. Lett.* **1996**, *77*, 3865–3868.
(33) Perdew, J. P.; Burke, K.; Ernzerhof, M. *Phys. Rev. Lett.* **1997**, *78*, 1396–1396.
(34) Handy, N. C.; Cohen, A. J. *Mol. Phys.* **2001**, *99*, 403–412.
(35) Lee, C. T.; Yang, W. T.; Parr, R. G. *Phys. Rev. B* **1988**, *37*, 785–789.
(36) Perdew, J. P.; Chevary, J. A.; Vosko, S. H.; Jackson, K. A.; Pederson, M. R.; Singh, D. J.; Fiolhais, C. *Phys. Rev. B* **1992**, *46*, 6671–6687.
(37) Noodleman, L.; Baerends, E. J. *J. Am. Chem. Soc.* **1984**, *106*, 2316–2327.
(38) Han, W.-G.; Liu, T.; Lovell, T.; Noodleman, L. *J. Am. Chem. Soc.* **2005**, *127*, 15778–15790.
(39) Klamt, A. *J. Phys. Chem.* **1995**, *99*, 2224–2235.
(40) Klamt, A.; Jonas, V. *J. Chem. Phys.* **1996**, *105*, 9972–9981.
(41) Klamt, A.; Schüürmann, G. *J. Chem. Soc., Perkin Trans. 2* **1993**, 799–805.
(42) Pye, C. C.; Ziegler, T. *Theor. Chem. Accounts* **1999**, *101*, 396–408.
(43) Shan, X.; Rohde, J. U.; Koehntop, K. D.; Zhou, Y.; Bukowski, M. R.; Costas, M.; Fujisawa, K.; Que, L. *Inorg. Chem.* **2007**, *46*, 8410–8417.

corresponding large structural shifts, we now think that model IV is less likely to represent the active site of the intermediate Q.

In this paper, we will establish our initial structures of the MMOH-P models (see Figure 2 for the O_2 binding patterns) mainly based on our MMOH-Q models I and II (Figure 3). The detailed structures of the MMOH-P models will be shown in Section 4.

3. Computational Methods

DFT methods have long been used in studying both organic and inorganic systems, and provide valuable and usually accurate predictions compared with experiment. However, the accuracy of the predictions, including geometries, relative energies, Mössbauer, and all other properties may vary with different exchange-correlation functionals for different systems. Therefore, we will utilize two functionals OPBE[32,33] and PW91[36] for current study, in order to have a better assessment of the calculated properties. Swart et al. have reported systematic studies on the performance of several exchange-correlation functionals for various properties of different systems.[44,45] They found that the OPBE potential correctly predicted the spin states for all the iron complexes they tested, and in general performs well in predicting other properties. The PW91 potential has been widely used in our group and demonstrated to be accurate in predicting various properties in our previous studies. Our main negative observations of PW91 potential are in our recent MMOH-Q calculations that it overestimated the Fe-ligand covalencies for models II and III (see Figure 3).[31] The net spin populations on the two iron sites for those models were only around 2 because of spin crossover. Consistently, the predicted quadrupole splitting values for models I−III were also much larger than the observed ones. However, in our current MMOH-P studies, no spin crossover problem occurred for the PW91 calculations, and the high-spin AF-coupled (or broken-symmetry[37,38] state) diiron sites were obtained for all intermediate P clusters by both OPBE and PW91 potentials.

The initial geometries of our Q models were taken or modified from the oxidized diferric crystal structure of MMOH from Mt OB3b protein.[30] In addition to the first-shell residues shown in Figure 3, we also included several second- and third-shell H-bonding residue side chains or main chain fragments. A $C_\beta-C_\alpha$ or $C_\gamma-C_\beta$ bond was broken and a linking hydrogen atom was added to fill the open valence of the terminal carbon atom.[46] These residues are: Glu114, His147, Glu144, His246, Glu209, Glu243, Gln140, Asn249, Asp143, Arg245, Asp242, Arg146, Ser238, and Val239 (see Figure 6 of ref 31 and Figure 4 of current paper). Some explicit water molecules are also included in the model clusters. All linking H atoms in the outer shell residue fragments Asn249, Arg245, Asp143, Asp242, Arg146, Ser238, and Val239 are fixed during the geometry optimizations. The initial structures of our current MMOH-P models are constructed based on the optimized Q models I and II, by modifying the O−O and Glu243 positions according to the core conformations in Figure 2.

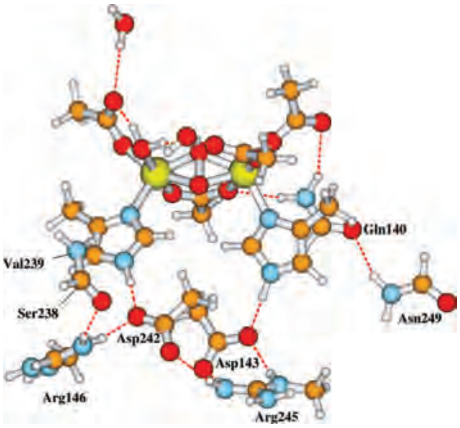

Figure 4. MMOH-P model with a terminal H_2O ($(H_2O)_t$) and a μ-η^2,η^2 O_2-binding conformation. The second- and third-shell H-bonding residues are labeled in the figure.

All models were geometry optimized within the COSMO[39–42] solvation model with dielectric constant $\epsilon = 4.0$ (representing the protein environment) and $\epsilon = 80.0$ (water) in ADF2005.01,[47–50] using broken-symmetry[37,38] DFT OPBE and PW91 functionals and triple-ξ plus polarization (TZP) Slater type basis sets (the inner core–shells of C(1s), N(1s), O(1s), and Fe(1s,2s,2p) were treated by the frozen core approximation during geometry optimizations). Cartesian coordinates of the linking H atoms in the outer shell residue fragments are also fixed as for the Q calculations.

To calculate the Mössbauer isomer (δ) shift and quadrupole splitting (ΔE_Q) properties, we then performed COSMO single-point energy calculations with all-electron TZP Slater type basis sets on the optimized geometries to obtain the electron density ($\rho(0)$) and the electric field gradient (EFG) at the Fe nucleus. Isomer shifts are then calculated as

$$\delta = \alpha(\rho(0) - A) + C \qquad (1)$$

In our previous studies,[31,51] the parameters α and C have been fitted separately for the $Fe^{2+,2.5+}$ and $Fe^{2.5+,3+,3.5+,4+}$ complexes for PW91, OPBE, and OLYP, with all-electron TZP Slater type basis sets. For the $Fe^{2.5+,3+,3.5+,4+}$ complexes, we have obtained $A = 11884.0$, $\alpha = -0.393$, and $C = 0.435$ mm s^{-1} for PW91 potential, and $A = 11877.0$, $\alpha = -0.312$, and $C = 0.373$ mm s^{-1} for OPBE method.

---

(44) Swart, M.; Groenhof, A. R.; Ehlers, A. W.; Lammertsma, K. *J. Phys. Chem. A* **2004**, *108*, 5479–5483.

(45) Swart, M.; Ehlers, A. W.; Lammertsma, K. *Mol. Phys.* **2004**, *102*, 2467–2474.

(46) Han, W.-G.; Tajkhorshid, E.; Suhai, S. *J. Biomol. Struct. Dyn.* **1999**, *16*, 1019–1032.

(47) *ADF 2005.01 SCM*; Vrije Universiteit: Amsterdam, The Netherlands; http://www.scm.com.

(48) Guerra, C. F.; Snijders, J. G.; te Velde, G.; Baerends, E. J. *Theor. Chem. Acc.* **1998**, *99*, 391–403.

(49) te Velde, G.; Bickelhaupt, F. M.; Baerends, E. J.; Guerra, C. F.; Van Gisbergen, S. J. A.; Snijders, J. G.; Ziegler, T. *J. Comput. Chem.* **2001**, *22*, 931–967.

(50) van Lenthe, E.; van der Avoird, A.; Wormer, P. E. S. *J. Chem. Phys.* **1998**, *108*, 4783–4796.

(51) Han, W. G.; Liu, T. Q.; Lovell, T.; Noodleman, L. *J. Comput. Chem.* **2006**, *27*, 1292–1306.

For calculating ΔE_Q, the EFG tensors V are diagonalized and the eigenvalues are reordered so that $|V_{zz}| \geq |V_{xx}| \geq |V_{yy}|$. The asymmetry parameter η is then defined as

$$\eta = |(V_{xx} - V_{yy})/V_{zz}| \tag{2}$$

Finally the quadrupole splitting for ^{57}Fe of the nuclear excited state ($I = 3/2$) can be calculated as

$$\Delta E_Q = ½eQV_{zz}(1 + \eta^2/3)^{1/2} \tag{3}$$

where e is the electrical charge of a positive electron, Q is the nuclear quadrupole moment (0.15 barns) of Fe.[52]

The BS state of the P models ($S_{Fe1} = S_{Fe2} = 5/2$ and $S_{total} = S_{min} = S_{Fe1} - S_{Fe2} = 0$) (with energy E_{BS}) obtained from DFT calculations is a mixture of pure spin states. To estimate the energy (E_0) of the pure spin ground state, we also performed a high-spin ferromagnetic (F) coupling COSMO single-point energy calculation ($S_{Fe1} = S_{Fe2} = 5/2$, and $S_{total} = S_{max} = S_{Fe1} + S_{Fe2} = 5$) on the BS state optimized geometry, and obtained the energy E_F. When the following Heisenberg (with Heisenberg coupling J) Hamiltonian H is applicable

$$H = -2J\mathbf{S_{Fe1}}\cdot\mathbf{S_{Fe2}} \tag{4}$$

the energy difference between F coupling and BS states can be described by

$$E_F - E_{BS} = -4JS_{Fe1}S_{Fe2} \tag{5}$$

And the pure-spin ground-state energy E_0 for the particular spin state (S_{Fe1}, S_{Fe2}) coupled to S_{min} according to the broken-symmetry geometry is estimated as

$$E_0 = E_F + JS_{max}(S_{max} + 1) - JS_{min}(S_{min} + 1) = E_F + 30J \tag{6}$$

where $S_{max} = 5$ and $S_{min} = 0$ for the current peroxo systems.

In the following, we will mainly present and analyze the calculations obtained with $\epsilon = 4.0$. The results obtained from $\epsilon = 80.0$ are given in the Supporting Information for comparison.

4. Models and Calculations for the Active Site of MMOH-P

4.1. μ-η^2,η^2 Models. Our μ-η^2,η^2 model with a terminal bound H_2O ($(H_2O)_t$), which is constructed from Q model II, is shown in Figure 4 with the second and third shell H-bonding residues labeled. Its central diiron structure is given in Figure 5. Because the second- and third-shell residues of other P models in current study are the same as those in Figure 4, we will show only the diiron core structures for other models hereafter. The structures shown here are obtained from OPBE geometry optimizations. The corresponding PW91 geometries are very similar. Our μ-η^2,η^2 model without the $(H_2O)_t$ coordinated to Fe1, which is constructed from Q model I, is given in Figure 6. This water moves into the second shell.

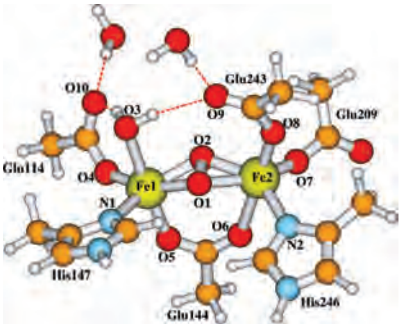

Figure 5. μ-η^2,η^2 peroxo-bridged diiron center of Figure 4, with the first-shell residues labeled.

The geometries, net-spin populations (NSP), broken-symmetry state energies (E_{BS}), spin-projected energies (E_0), Heisenberg J values, Mössbauer isomer shifts (δ), quadrupole splittings (ΔE_Q), and η values of the two μ-η^2,η^2 peroxo models calculated from OPBE and PW91 potentials with $\epsilon = 4.0$ are given in Table 1. The corresponding results calculated with $\epsilon = 80.0$ are given in Table S3 of the Supporting Information. As observed from MMOH-Q calculations,[31] PW91 potential produces shorter Fe–Fe distances, and usually shorter Fe-ligand distances and stronger hydrogen bonding interactions than OPBE method. The calculated net-spin populations (about 4) from both functionals clearly show the $S_{Fe1} = S_{Fe2} = 5/2$ AF-coupled (or BS) state for the two models. When there is no terminal water bonding to Fe1, atom O6 (see Figure 6) in Glu144 also dissociates from Fe2 (but still H-bonds to Gln140 as shown in Figure 4), and both Fe^{3+} sites have 5 ligands.

4.2. *trans*-μ–1,2 Peroxo Models. Many *trans*-peroxo local minima can exist, with O1 or O2 in the space between His147 and His246 or between Glu114 and Glu209 (see Figure 2), with or without the $(H_2O)_t$, and with O1–O2 in (or nearly in) the plane with Fe1 and Fe2 or out of the plane. Two representable conformations (distinguished by “a” and “b”) obtained by the two DFT potentials will be presented here, and their diiron first-shell centers are shown in Figures 7 and 8. The OPBE and PW91 calculated properties in $\epsilon = 4.0$ are given in Table 2.

The initial structure of model *trans*-μ–1,2a (Figure 7) was set up from the μ-η^2,η^2 model in Figure 5 by shifting the O–O to *trans*-position. In OPBE calculation, during the geometry optimization, the Fe1–Fe2 distance is increased by 0.908 Å. The $(H_2O)_t$ and O6 of Glu144 dissociate from Fe1 and Fe2, respectively. In PW91 calculations, the $(H_2O)_t$ loosely binds to Fe1 in the $\epsilon = 4.0$ optimized *trans*-μ–1,2a structure with a bonding distance of 2.329 Å.

Another *trans*-μ–1,2 peroxo model (*trans*-μ–1,2b, Figure 8) we present here is derived from a *cis*-μ–1,2 geometry optimization in both OPBE and PW91 calculations, where the latter starts from the μ-η^2,η^2 model in Figure 6. Our initial purpose was to see if the *cis*-μ–1,2 structure can exist as a stable intermediate when the $(H_2O)_t$ already has dissociated from Fe1. We deleted the central O–O atoms from Figure 6 and put them in the *cis*-μ–1,2 position (O1, O2, Fe1, and Fe2 are in the same plane) in the space between Glu114 and Glu209. However, during the geometry optimizations (in both OPBE and PW91 and both $\epsilon = 4.0$ and $\epsilon = 80.0$), O1 (connecting to Fe1) turns up and moves in, and O2 (bonding

---

[52] Martinez-Pinedo, G.; Schwerdtfeger, P.; Caurier, E.; Langanke, K.; Nazarewicz, W.; Sohnel, T. *Phys. Rev. Lett.* **2001**, *87*, 062701/1–4.

Table 1. Geometries (Å and deg), Net-Spin Populations (NSP), Broken-Symmetry State Energies (E_{BS}), Spin-Projected Energies (E_0, eV), Heisenberg J Values (cm^{-1}), Mössbauer Isomer Shifts (δ, mm s^{-1}), Quadrupole Splittings (ΔE_Q, mm s^{-1}), and η Values Calculated from OPBE and PW91 Functionals with $\epsilon = 4.0$ for the μ-η^2,η^2 MMOH-Peroxo Active Site Models with and without a Terminal (t) H_2O (Figures 4–6), and Compared with Available Experimental Values

	with $(H_2O)_t$ (Figures 4 and 5)		without $(H_2O)_t$ (Figure 6)		
	OPBE	PW91	OPBE	PW91	exp.[8]
		Geometry			
Fe1−Fe2	3.618	3.575	3.688	3.627	
Fe1−O1	2.045	2.018	2.067	2.037	
Fe2−O1	2.022	2.026	1.977	1.973	
Fe1−O2	1.984	2.004	1.947	1.959	
Fe2−O2	2.007	1.958	2.031	2.005	
O1−O2	1.444	1.483	1.452	1.494	
Fe1−O3	2.295	2.256	5.492	4.881	
Fe1−O4	1.962	1.950	1.903	1.899	
Fe1−N1	2.143	2.075	2.128	2.080	
Fe1−O5	1.978	2.000	1.915	1.921	
Fe2−O6	2.406	2.273	3.644	3.179	
Fe2−N2	2.141	2.084	2.113	2.064	
Fe2−O7	1.907	1.900	1.897	1.896	
Fe2−O8	1.952	1.970	1.905	1.919	
∠Fe1−O1−Fe2	125.7	124.3	131.5	129.5	
∠Fe1−O2−Fe2	130.1	128.9	136.0	132.4	
∠Fe1−O2−O1−Fe2	148.4	148.2	161.0	157.8	
O3···O9	3.459	3.011	3.156	2.743	
O3···O10	2.690	2.700	3.101	2.784	
NSP_{Fe1}	4.05	3.99	4.04	3.94	
NSP_{Fe2}	−4.00	−3.92	−4.02	−3.92	
E_{BS}	−743.5884	−741.4884	−743.7477	−741.3098	
E_0	−743.6469	−741.5697	−743.8278	−741.4128	
J	−94	−131	−129	−166	
		Mössbauer Parameters			
δ_{Fe1}	0.59	0.64	0.56	0.60	0.66
δ_{Fe2}	0.59	0.61	0.54	0.57	
ΔE_Q(Fe1)	−0.48	−0.70	0.47	−0.57	1.51
ΔE_Q(Fe2)	−0.76	0.81	−0.87	−0.97	
η(Fe1)	0.80	0.66	0.99	0.80	
η(Fe2)	0.95	0.95	0.58	0.74	

to Fe2) turns down, so that the directions of four ligands of Fe1 and Fe2 tend to form the tetrahedron-like conformations. This indicates that if the $(H_2O)_t$ dissociates from Fe1, a *cis*-μ−1,2 O−O binding mode will change to a *trans*-μ−1,2 conformation.

4.3. *cis*-μ−1,2 Peroxo Models. Also two *cis*-μ−1,2 peroxo structures are studied here, one (*cis*-μ−1,2a in Figure 2) having a mono-oxygen bridge from Glu243 as in the reduced diferrous MMOH state (see Figure 1), and another (*cis*-μ−1,2b in Figure 2) with the Glu243 H-bonding to the $(H_2O)_t$ as in the MMOH diferric state. Similar models were also studied by other groups.[6,16] In our model *cis*-μ−1,2a, we shift a water molecule to H-bond to the $(H_2O)_t$. This H_2O is comparable to the one H-bonding to O9 of Glu243 in other models. Each active site model has the same number of explicit water molecules and same composition and number of atoms (123), so that we can compare their energies. The central diiron fragments of our *cis*-μ−1,2a and *cis*-μ−1,2b models are shown in Figures 9 and 10, respectively. Their OPBE and PW91 calculated properties for $\epsilon = 4.0$ are given in Table 3.

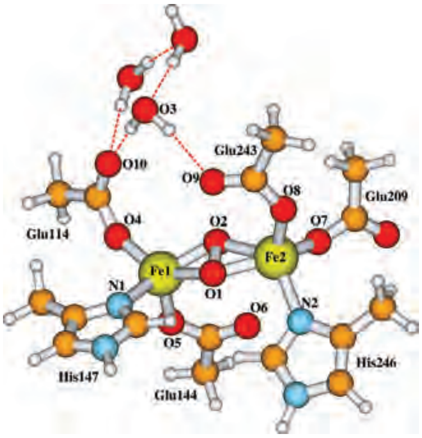

Figure 6. Peroxo-bridged diiron center of our μ-η^2,η^2 model without the $(H_2O)_t$. The second- and third-shell H-bonding residues are shown in Figure 4.

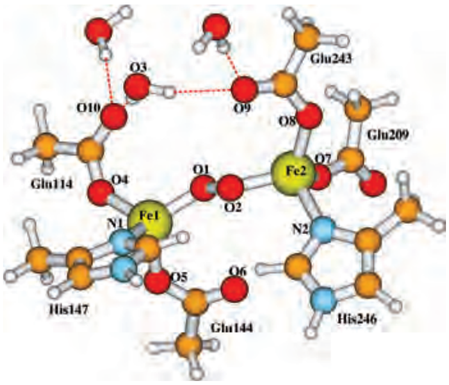

Figure 7. Peroxo-bridged diiron center of our *trans*-μ−1,2a model. The second- and third-shell H-bonding residues are the same as shown in Figure 4.

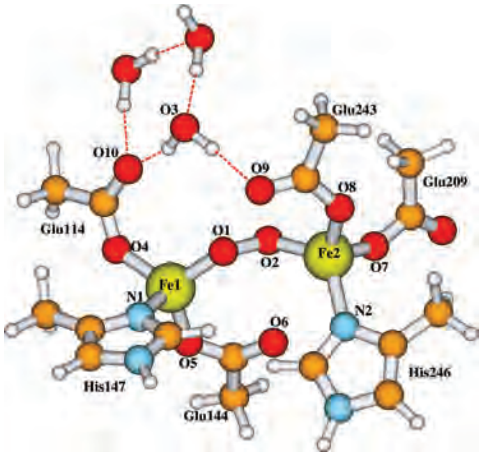

Figure 8. Peroxo-bridged diiron center of our *trans*-$\mu-1,2$b model. The second- and third-shell H-bonding residues are the same as shown in Figure 4.

4.4. Calculated and Experimental Property Comparisons. Experimentally only one set of Mössbauer isomer shift (0.66 mm s^{-1}) and quadrupole splitting (1.51 mm s^{-1}) was observed. To compare our predicted Mössbauer properties among all the MMOH-P models and with the experiment, we averaged the calculated isomer shifts and quadrupole splittings of the two iron sites in each model for both OPBE and PW91 calculations. The comparisons are given in Figures 11 and 12. Experimentally, no η value was reported for the quadrupole splitting measurement. Our calculations show that the quadrupole splitting signs can be changed by the environment and the different computational methods or atomic basis sets. We therefore mainly focused on the absolute values of the quadrupole splittings when comparing our calculations with experiment.

Although the absolute values of the Mössbauer properties for a certain model are predicted differently by the two methods, the overall relative trends are predicted similarly. For isomer shifts, both methods predict the smallest values for the *trans*-$\mu-1,2$ models, which are the farthest from the experiment, then followed by the two μ-η^2,η^2 models, and then the two *cis*-$\mu-1,2$ models. For quadrupole splittings, the μ-η^2,η^2 models are predicted to be the worst, then the *trans*-$\mu-1,2$ results are closer to experiment, and then the *cis*-$\mu-1,2$ models again the closest to the experiment. Therefore our Mössbauer calculations indicate that the *cis*-$\mu-1,2$ models best represent the active site of MMOH intermediate P. Considering the similarity of the two iron sites from the Mössbauer experiment, the *cis*-$\mu-1,2$b model is a little better than *cis*-$\mu-1,2$a (see Table 3). However, to determine which model is the best to represent MMOH-P, we also need to compare their relative energies.

Kinetically, it was reported that the MMOH-P forms with a rate constant of ~9–12 s^{-1} and decays (therefore forming intermediate Q) with a rate constant of ~2.5 s^{-1} at 4 °C, pH 7 for Mt protein.[53,54] The activation parameter (E_a) for P → Q is about 28 kcal mol^{-1} for Mt and about 27 kcal mol^{-1} for Mc protein.[8,54] Kinetic analysis using E_a and the observed Arrhenius preexponential factor A as well yields transition state theory activation parameters of: (for Mt), $\Delta H^\ddagger = 27.3$ kcal mol^{-1}; $\Delta S^\ddagger = 44.3$ cal mol^{-1} K^{-1}; $\Delta G^\ddagger = 14.1$ kcal mol^{-1} (at $T = 298$ K); (for Mc), $\Delta H^\ddagger = 26.5$ kcal mol^{-1}; $\Delta S^\ddagger = 35.1$ cal mol^{-1} K^{-1}; $\Delta G^\ddagger = 16$ kcal mol^{-1}, whereas the enthalpic barrier is substantial ($\Delta H^\ddagger$), the entropy change ($\Delta S^\ddagger$) for activating P is strongly positive and favorable ($-T\Delta S^\ddagger$ is negative and about -13 to -10.5 kcal mol^{-1}). Therefore, the kinetically observed intermediate P must be a stable state with relatively low energy. Further, the transition state following P (for the formation of Q, P → Q) displays the large activation entropy increase discussed above, and therefore has a more open structure than intermediate P. These observations are consistent with the early stages of the P → Q reaction pathway we will explore. We there compare the relative energies (relative to *cis*-$\mu-1,2$a) of all the MMOH-P models in Figure 13. The relative energies in both OPBE and PW91 calculations of our favorable MMOH-Q model (model II in Figure 3) are also given in Figure 13.

From Tables 1, 2, 3 and Figure 13, we see that the OPBE and PW91 calculations predict different relative energies for these model structures. These energies are also different from recent B3LYP calculations, which predicted that the μ-η^2,η^2 model had the lowest energy.[6] For transition metal complexes, obtaining converged and consistent results with different potentials of DFT is at present still a great challenge. Calculating the full transition states and the transition barriers, which have not yet been performed in the current study, are also very challenging. We have, however, performed reaction coordinate driven optimizations that are highly relevant, presented in the next section (Section 5). With these difficulties in mind, we need to see what is in common obtained by different potentials, and to calculate and compare results not only for one property, but if possible for all relevant properties.

Both OPBE and PW91 calculations predict that model *cis*-$\mu-1,2$b has the highest energy among all the P-models studied here. *cis*-$\mu-1,2$a is significantly lower in energy than *cis*-$\mu-1,2$b by 10.5 and 12.0 kcal mol^{-1} in OPBE and PW91 calculations, respectively. In fact, the *cis*-$\mu-1,2$a model has the lowest energy in PW91 calculations among all the MMOH-P models in both $\epsilon = 4.0$ and 80.0 environments. The OPBE potential predicts that the electronic energies of the *trans*-$\mu-1,2$ models are much lower than *cis*-$\mu-1,2$a. However, the predicted Mössbauer properties of the *trans*-$\mu-1,2$ models are far from experiment. We therefore do not think that the *trans*-$\mu-1,2$ models are the kinetically identified P state. On the other hand, *cis*-$\mu-1,2$a is also a low energy stable structure and is much closer to the MMOH diferrous state (see Figure 1) than any other models studied here, it is therefore very likely that the molecular oxygen binds to the reduced MMOH in the *cis*-$\mu-1,2$a form by only pushing away the second water-ligand that is in the space between Glu114 and Glu209 in the diferrous center (Figure 1). From *cis*-$\mu-1,2$a to other (for instance *trans* and μ-η^2,η^2) structures or to MMOH-Q, the carboxylate group of Glu243 has to move up to the position in *cis*-$\mu-1,2$b. This requires

---

(53) Lee, S. Y.; Lipscomb, J. D. *Biochemistry* **1999**, *38*, 4423–4432.
(54) Brazeau, B. J.; Lipscomb, J. D. *Biochemistry* **2000**, *39*, 13503–13515.

Table 2. Geometries (Å and degree), Net-Spin Populations (NSP), Broken-Symmetry State Energies (E_{BS}), Spin-Projected Energies (E_0) (eV), Heisenberg J Values (cm^{-1}), Mössbauer Isomer Shifts (δ) (mm s^{-1}), Quadrupole Splittings (ΔE_Q) (mm s^{-1}), and η Values Calculated from OPBE and PW91 Functionals with $\epsilon = 4.0$ for the *trans*-μ−1,2a (Figure 7) and *trans*-μ−1,2b (Figure 8) MMOH-Peroxo Active Site Models.

	trans-μ−1,2a (Figure 7)		*trans*-μ−1,2b (Figure 8)		
	OPBE	PW91	OPBE	PW91	exp.[8]
		Geometry			
Fe1−Fe2	4.526	4.357	4.665	4.441	
Fe1−O1	1.870	1.886	1.903	1.846	
Fe2−O2	1.877	1.863	1.910	1.874	
O1−O2	1.358	1.400	1.358	1.370	
Fe1−O3	4.539	2.329	4.996	4.701	
Fe1−O4	1.909	1.959	1.904	1.920	
Fe1−N1	2.075	2.069	2.188	2.039	
Fe1−O5	1.934	1.965	1.938	1.917	
Fe2−O6	4.233	3.971	4.282	3.555	
Fe2−N2	2.076	2.029	2.151	2.045	
Fe2−O7	1.879	1.876	1.879	1.877	
Fe2−O8	1.915	1.921	1.921	1.919	
∠Fe1−O1−O2	120.4	102.2	121.3	127.8	
∠Fe2−O2−O1	120.0	114.0	128.5	118.0	
∠Fe1−O1−O2−Fe2	154.6	168.8	−154.2	−135.2	
O3···O9	3.227	3.320	3.339	2.811	
O3···O10	3.194	2.658	3.121	2.807	
NSP_{Fe1}	4.06	4.00	4.05	3.93	
NSP_{Fe2}	−4.01	−3.93	−4.01	−3.94	
E_{BS}	−744.0681	−741.3687	−743.8837	−741.2110	
E_0	−744.1095	−741.4146	−743.9232	−741.2665	
J	−67	−74	−64	−90	
		Mössbauer Parameters			
δ_{Fe1}	0.48	0.56	0.54	0.53	0.66
δ_{Fe2}	0.49	0.50	0.53	0.52	
ΔE_Q(Fe1)	1.12	1.21	−1.07	0.82	1.51
ΔE_Q(Fe2)	1.00	0.96	−0.47	0.87	
η(Fe1)	0.31	0.57	0.79	0.12	
η(Fe2)	0.08	0.29	0.28	0.86	

more than 12 kcal mol^{-1}, since the electronic energy difference between *cis*-μ−1,2a and *cis*-μ−1,2b is already predicted as 10.5 and 12.0 kcal mol^{-1} in OPBE and PW91 calculations. Because of this large barrier for *cis*-μ−1,2a transforming to other conformations, *cis*-μ−1,2a can be accumulated in low temperature and hence identified by the kinetic freeze-quench Mössbauer spectroscopy.[8] We therefore propose that the *cis*-μ−1,2a model represents the active site of the kinetically identified MMOH-peroxo intermediate P. This is also in agreement with the vibrational analysis reported by Yoshizawa and Solomon's groups, which show that the calculated O−O stretching vibrations in the *cis*-μ−1,2 peroxo models fall within the range measured in peroxo intermediates of other nonheme diiron enzymes and *cis*-μ−1,2 peroxo-bridged diiron(III) synthetic complexes.[16,17] Further, the MMOH-P structure proposed by Yoshizawa's group based on their energetic and frequency calculations is the same as our *cis*-μ−1,2a model.[16]

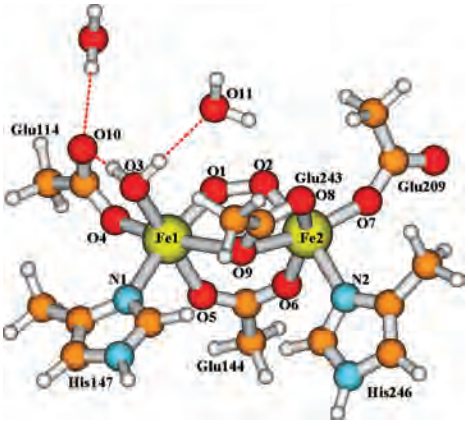

Figure 9. Central fragment of our *cis*-μ−1,2a model. The second- and third-shell H-bonding residues are the same as shown in Figure 4.

5. Feasible P → Q Pathway

If *cis*-μ−1,2a structure does represent the active site of MMOH intermediate P, how can this structure change to another intermediate, MMOH-Q (see model II in Figure 3 for our Q model)? Comparing the two structures, the Glu243 side chain in *cis*-μ−1,2a has to move up from the mono-oxygen bridging position to leave the room for one of the O atom in O_2 moving across the Fe1−Fe2 line in order to form

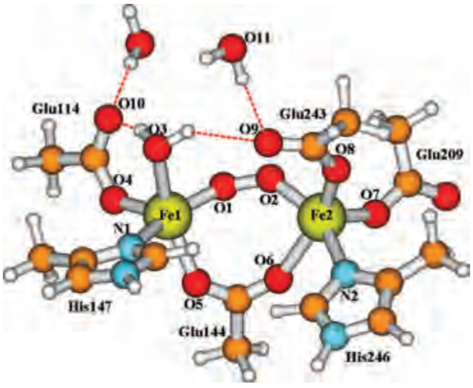

Figure 10. Central fragment of our *cis*-μ−1,2b model. The second- and third-shell H-bonding residues are the same as shown in Figure 4.

Table 3. Geometries (Å and degree), Net-Spin Populations (NSP), Broken-Symmetry State Energies (E_{BS}), Spin-Projected Energies (E_0) (eV), Heisenberg J Values (cm^{-1}), Mössbauer Isomer Shifts (δ) (mm s^{-1}), Quadrupole Splittings (ΔE_Q) (mm s^{-1}), and η Values Calculated from OPBE and PW91 Functionals with ϵ = 4.0 for the *cis*-μ−1,2a (Figure 9) and *cis*-μ−1,2b (Figure 10) MMOH-Peroxo Active Site Models

	cis-μ−1,2a (Figure 9)		*cis*-μ−1,2b (Figure 10)		
	OPBE	PW91	OPBE	PW91	exp.[8]
		Geometry			
Fe1−Fe2	3.768	3.642	4.234	3.944	
Fe1−O1	1.878	1.893	1.887	1.889	
Fe2−O2	1.928	1.888	1.941	1.888	
Fe1−O9	2.634	2.333			
Fe2−O9	2.220	2.239			
O1−O2	1.328	1.360	1.332	1.358	
Fe1−O3	2.174	2.164	2.221	2.141	
Fe1−O4	2.007	2.008	1.942	1.939	
Fe1−N1	2.218	2.174	2.260	2.126	
Fe1−O5	2.072	2.075	2.041	2.026	
Fe2−O6	2.097	2.108	2.220	2.166	
Fe2−N2	2.217	2.141	2.253	2.113	
Fe2−O7	1.919	1.899	1.898	1.909	
Fe2−O8	2.186	2.227	1.965	1.978	
∠Fe1−O1−O2	136.3	130.3	138.3	128.0	
∠Fe2−O2−O1	123.6	123.6	132.8	128.2	
∠Fe1−O1−O2−Fe2	7.0	9.8	52.8	55.8	
O3···O9			3.350	2.675	
O3···O10	2.570	2.594	2.645	2.759	
O3···O11	3.071	2.804			
NSP$_{Fe1}$	3.97	3.91	3.99	3.91	
NSP$_{Fe2}$	−3.98	−3.84	−4.05	−3.91	
E_{BS}	−743.5659	−741.7140	−743.1156	−741.2079	
E_0	−743.6155	−741.7845	−743.1610	−741.2650	
J	−80	−114	−73	−92	
		Mössbauer Parameters			
δ_{Fe1}	0.66	0.72	0.69	0.64	0.66
δ_{Fe2}	0.59	0.63	0.64	0.61	
ΔE_Q(Fe1)	−1.81	−1.69	1.62	−1.81	1.51
ΔE_Q(Fe2)	−0.79	−1.12	1.00	−1.21	
η(Fe1)	0.65	0.49	0.80	0.98	
η(Fe2)	0.14	0.26	0.72	0.83	

the di-μ-oxo bridges in Q. It is likely that the *cis*-μ−1,2a → *cis*-μ−1,2b would be the first step of the structural changes in the P → Q pathway. Although there is no direct evidence that both of the oxygen atoms in the di-μ-oxo bridges of Q derive from a single O$_2$, it is a reasonable assumption and has been treated this way in all theoretical calculations.

Recalling the formation of our *trans*-μ−1,2b model (section 4.2, Figure 8), we see that if the (H$_2$O)$_t$ and O6 of Glu144 dissociate from Fe1 and Fe2, respectively, a side-on *cis*-μ−1,2b conformation of O1−O2 will automatically change to a *trans*-μ−1,2 conformation required by the 4-ligand binding configurations of both Fe1 and Fe2. The two μ-oxo bridges can be readily formed by breaking the O1−O2 bond in the *trans*-μ−1,2 fashion. We therefore propose that after or at the same time as *cis*-μ−1,2a → *cis*-μ−1,2b transformation, the (H$_2$O)$_t$ ligand should dissociate from Fe1 and O6 in Glu144 should dissociate from Fe2. In all X-ray crystal structures of MMOH, O6 of Glu144 also H-bonds to H−N of Gln140 side chain, O6 is far from Fe2, and Fe2−O6 has the longest distance (r) among all Fe−O-carboxylate distances. r(Fe2−O6) = 2.29 Å in the diferric

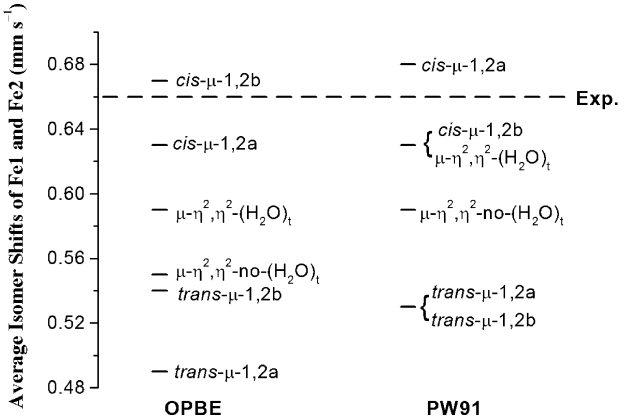

Figure 11. Average of the calculated isomer shifts for sites Fe1 and Fe2 of each MMOH-P model calculated in both OPBE and PW91 methods and compared with experiment.

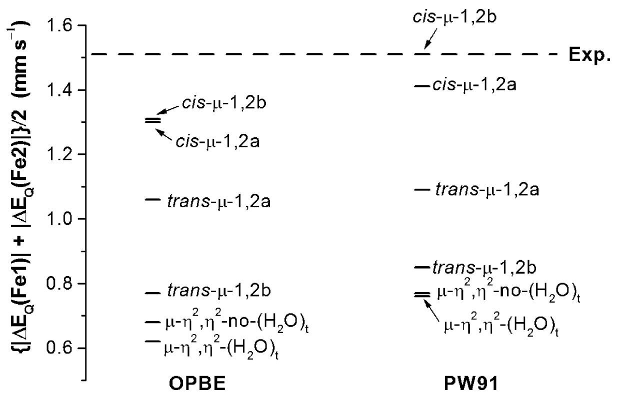

Figure 12. Average of the absolute values of the calculated quadrupole splittings for sites Fe1 and Fe2 of each MMOH-P model calculated in both OPBE and PW91 methods and compared with experiment.

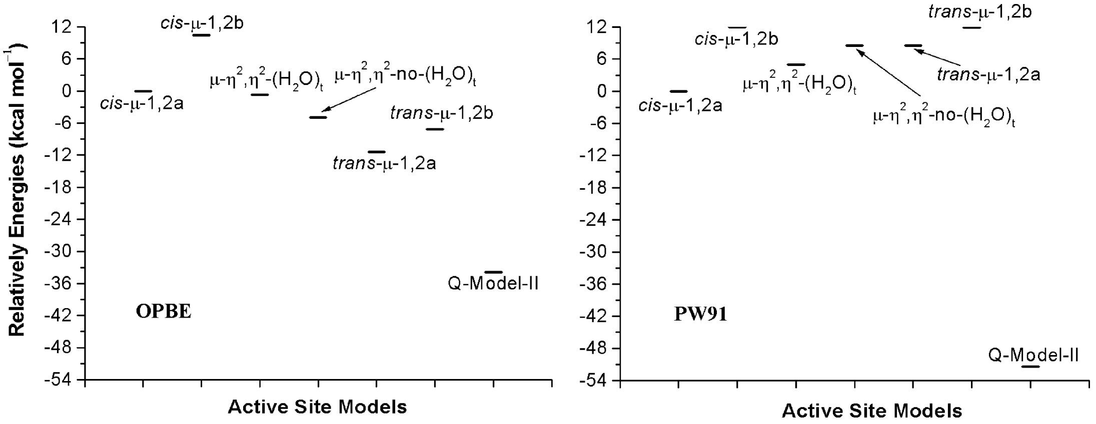

Figure 13. Comparison of relative energies of all MMOH-P models and MMOH-Q model II (see Figure 3) in both OPBE and PW91 calculations. Energies are relative to model *cis*-μ−1,2a.

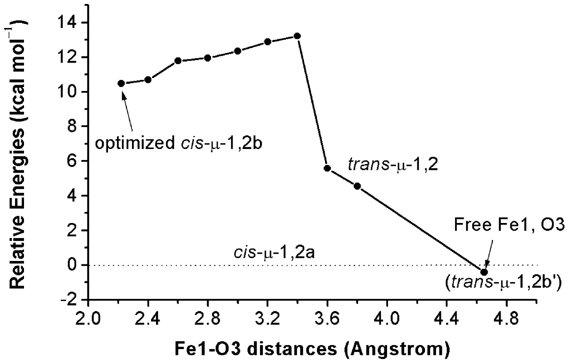

Figure 14. Energies of the OPBE partially optimized (in COSMO with ϵ = 4.0) *cis*-μ−1,2b geometries with fixed Fe1 and O3 Cartesian coordinates relative to the energy of the optimized *cis*-μ−1,2a structure.

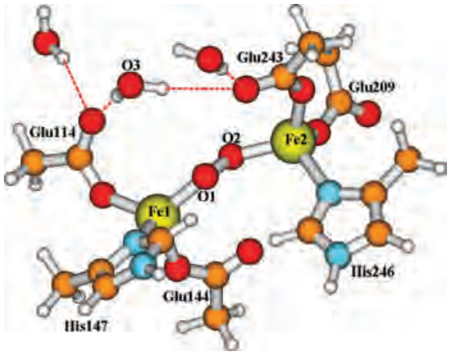

Figure 16. Optimized structure (*trans*-μ−1,2b′) obtained by relaxing both Fe1 and O3 atoms in the partially optimized structure with fixed r(Fe1−O3) = 3.8 Å (see Figure 15). The second and third shell H-bonding residues are the same as shown in Figure 4.

active site of MMOH from Mt, 2.44 Å in the diferric structure from Mc, and 2.39 Å in the diferrous state.[29,30] Other Fe−O-carboxylate distances, for instance in the MMOH(Mt) diferric state X-ray crystal structure, are r(Fe1−O4) = 1.89 Å, r(Fe1−O5) = 2.05 Å, r(Fe2−O7) = 2.01 Å, and r(Fe2−O8) = 1.86 Å.

In order to estimate the energy cost of the $(H_2O)_t$ dissociating from Fe1, starting from the OPBE (in COSMO with ϵ = 4.0) optimized *cis*-μ−1,2b structure (Figure 10), we moved the $(H_2O)_t$ away from Fe1 along the Fe1−O3 direction to the positions of r(Fe1−O3) = 2.4 Å, 2.6 Å, ... increments with 0.2 Å interval to 3.8 Å. We then optimized these *cis*-μ−1,2 structures using OPBE functional (still in COSMO with ϵ = 4.0) with fixed Fe1 and O3 xyz coordinates (H-linking atoms in outer shell were also fixed as in all other geometry optimizations). Because all our other geometry optimizations were performed in Cartesian coordinates with the outer shell H-linking atoms fixed, we can not only fix the r(Fe1−O3) distance and optimize the rest. Therefore, the energies and geometries obtained from these (fixed Fe1, O3) partial optimizations do not reflect the full $(H_2O)_t$ dissociation pathway. The aim of these calculations is just to estimate the $(H_2O)_t$ dissociation energy and to see how the *cis*-μ−1,2b O1−O2 binding conformation changes and if O6 of Glu144 will also dissociate from Fe2 upon the dissociation of $(H_2O)_t$. The energies of these structures

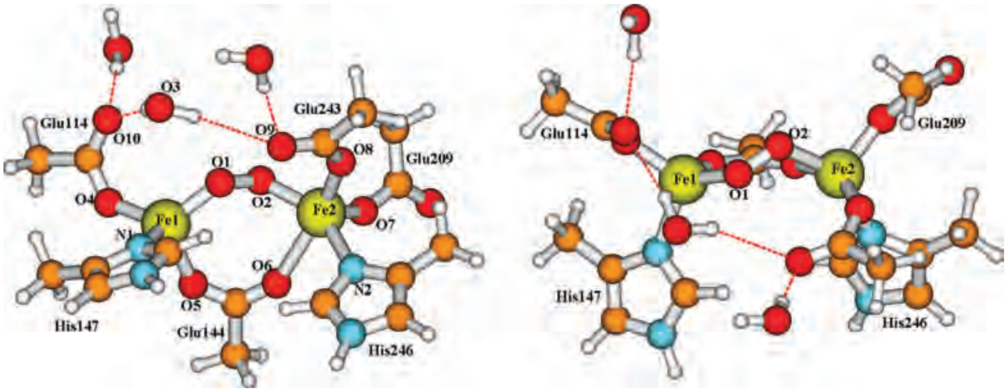

Figure 15. Diiron center of the OPBE partially optimized structure (starting from optimized *cis*-μ−1,2b and positions of Fe1 and O3 were fixed) with r(Fe1−O3) = 3.8 Å. Left: side view. Right: view from top. The second and third shell H-bonding residues are the same as shown in Figure 4.

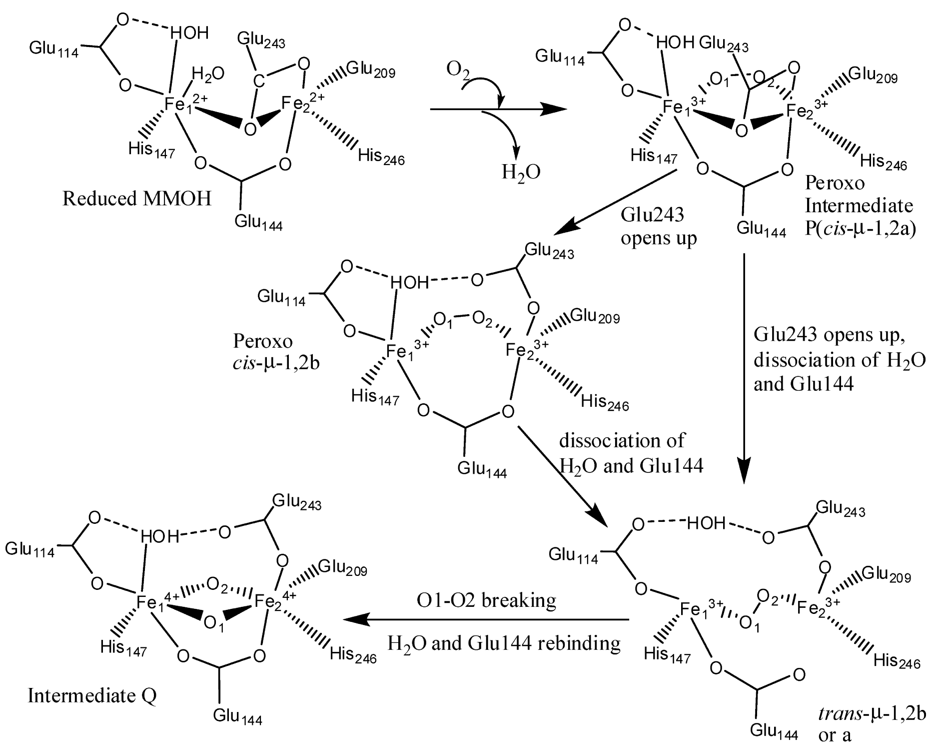

Figure 17. Proposed structurally and energetically feasible conformational changes along the P → Q transform pathway.

relative to the optimized *cis*-μ−1,2a model (Figure 9) obtained from OPBE calculation are shown in Figure 14.

The r(Fe1−O3) = 3.4 Å structure has the highest relative energy (2.7 kcal mol^{-1} higher than optimized *cis*-μ−1,2b, and 13.2 kcal mol^{-1} higher than *cis*-μ−1,2a). Within our current theoretical/computational model, this *cis*-μ−1,2b like transient state at $\Delta E^{\ddagger} = 13.2$ kcal mol^{-1} represents our best approximation to the transition state. The calculated approximate activation barrier is well below the experimental activation enthalpy of $\Delta H^{\ddagger} = 26$ to 27 kcal mol^{-1}. The qualitative change from *cis*-μ−1,2a to *cis*-μ−1,2b and similar subsequent states is consistent with a substantial activation entropy. The energy of the next structure with r(Fe1−O3) = 3.6 Å drops substantially and is lower than the initial optimized *cis*-μ−1,2b by 4.9 kcal mol^{-1}. The structure with r(Fe1−O3) = 3.8 Å then further drops by 1.0 kcal mol^{-1}. Therefore in OPBE calculations, the energy cost for dissociating the $(H_2O)_t$ from *cis*-μ−1,2b is not much higher than 2.7 kcal mol^{-1}. The fixed (Fe1,O3) partially optimized structures with r(Fe1−O3) ≤ 3.4 Å still remain in the *cis*-μ−1,2 mode. However, the structures with r(Fe1−O3) = 3.6 and 3.8 Å during the geometry optimizations change to the out-of-plane *trans* form with atom O1 moving in as in *trans*-μ−1,2b. Figure 15 shows the diiron center of the partially optimized structure with fixed r(Fe1−O3) = 3.8 Å looking from the side and looking from the top. Atom O6 very loosely binds with Fe2 with a long distance of 2.359 Å.

Starting from this partially optimized r(Fe1−O3) = 3.8 Å structure, we let both Fe1 and O3 optimize freely (still using OPBE functional and ϵ =4.0 in COSMO). The $(H_2O)_t$ moved further away from Fe1 to r(Fe1−O3) = 4.65 Å, and its energy lowered by 5.0 kcal mol^{-1} (see the last point in Figure 14). The central diiron structure is shown in Figure 16. We call this structure as *trans*-μ−1,2b′ because it looks very similar to *trans*-μ−1,2b shown in Figure 8. The main structural difference between *trans*-μ−1,2b′ and *trans*-μ−1,2b is the orientation of the three water molecules. Therefore, the dissociation of the $(H_2O)_t$ from Fe1 does change the O1−O2 binding mode from cis to trans-like conformation. Atom O6 in the carboxylate group of Glu144 also dissociates from Fe2 automatically.

The energy of *trans*-μ−1,2b′ is 0.4 kcal mol^{-1} below *cis*-μ−1,2a (see Figure 14), and by 33.5 kcal mol^{-1} above our proposed MMOH-Q model (see OPBE results in Figure 13).[31] The breaking of O1−O2 bond will then lead the *trans*-μ−1,2 form to intermediate Q with μ-O1 and μ-O2 bridges and the association of the $(H_2O)_t$ and O6 back to Fe1 and Fe2. It is still an open question how O1−O2 bond breaks. Protons may play roles in the O−O cleavage process. However, with such large energy difference between *trans*-μ−1,2b′ and Q, it also looks favorable for *trans*-μ−1,2b′ to transform to Q directly without protons.

The transformation of *cis*-μ−1,2b → *trans*-μ−1,2a (Figure 7) may also be a potential pathway, since *trans*-μ−1,2a is more stable than *trans*-μ−1,2b. The transition pathway and barrier are not obtained yet. The *trans*-μ−1,2a model is by 11.4 kcal mol^{-1} lower than *cis*-μ−1,2a, and by 22.5 kcal mol^{-1} higher than our proposed MMOH-Q model in OPBE calculations. The *trans*-μ−1,2b in OPBE is by 7.1 kcal mol^{-1} lower than *cis*-μ−1,2a. Our proposed P → Q pathway is schematically given in Figure 17.

6. Comparison of ϵ = 4.0 and ϵ = 80.0 Calculations

All results in Tables 1−3 are also calculated with ϵ = 80.0 and are given in Tables S3−S5 of the Supporting Information. The predicted isomer shifts for each model cluster are almost the same in the two kinds of environment. The signs and η values of some predicted quadrupole splittings change when changing the solvent dielectric constant. But the absolute values of the quadrupole splittings are very similar in the two conditions.

From $\epsilon = 4.0$ to $\epsilon = 80.0$, the electronic energies drop by about 2 eV. The relative energies among different P models also change. In OPBE, the order of the relative energies change from $E_0(\textit{trans}\text{-}\mu{-}1\text{,}2\text{a}) < E_0(\textit{trans}\text{-}\mu{-}1\text{,}2\text{b}) < E_0(\mu\text{-}\eta^2\text{,}\eta^2\text{-no-}(\mathrm{H_2O})_\mathrm{t}) < E_0(\mu\text{-}\eta^2\text{,}\eta^2\text{-}(\mathrm{H_2O})_\mathrm{t}) < E_0(\textit{cis}\text{-}\mu{-}1\text{,}2\text{a}) < E_0(\textit{cis}\text{-}\mu{-}1\text{,}2\text{b})$ to $E_0(\textit{trans}\text{-}\mu{-}1\text{,}2\text{a}) < E_0(\textit{trans}\text{-}\mu{-}1\text{,}2\text{b}) < E_0(\mu\text{-}\eta^2\text{,}\eta^2\text{-no-}(\mathrm{H_2O})_\mathrm{t}) < E_0(\textit{cis}\text{-}\mu{-}1\text{,}2\text{a}) < E_0(\mu\text{-}\eta^2\text{,}\eta^2\text{-}(\mathrm{H_2O})_\mathrm{t}) < E_0(\textit{cis}\text{-}\mu{-}1\text{,}2\text{b})$. In PW91, this relative energy order changes from $E_0(\textit{cis}\text{-}\mu{-}1\text{,}2\text{a}) < E_0(\mu\text{-}\eta^2\text{,}\eta^2\text{-}(\mathrm{H_2O})_\mathrm{t}) < E_0(\textit{trans}\text{-}\mu{-}1\text{,}2\text{a}) < E_0(\mu\text{-}\eta^2\text{,}\eta^2\text{-no-}(\mathrm{H_2O})_\mathrm{t}) < E_0(\textit{trans}\text{-}\mu{-}1\text{,}2\text{b}) < E_0(\textit{cis}\text{-}\mu{-}1\text{,}2\text{b})$ to $E_0(\textit{cis}\text{-}\mu{-}1\text{,}2\text{a}) < E_0(\textit{trans}\text{-}\mu{-}1\text{,}2\text{a}) < E_0(\mu\text{-}\eta^2\text{,}\eta^2\text{-}(\mathrm{H_2O})_\mathrm{t}) < E_0(\mu\text{-}\eta^2\text{,}\eta^2\text{-no-}(\mathrm{H_2O})_\mathrm{t}) < E_0(\textit{trans}\text{-}\mu{-}1\text{,}2\text{b}) < E_0(\textit{cis}\text{-}\mu{-}1\text{,}2\text{b})$. Most of the P models have very similar geometries in the two kinds of dielectric environment. In $\epsilon = 80.0$, for *trans*-μ−1,2a model, the PW91 potential also prefers a nonbonded $(\mathrm{H_2O})_\mathrm{t}$ with Fe1−O3 distance 4.064 Å. However, in nonpolar $\epsilon = 4$ environment, this $(\mathrm{H_2O})_\mathrm{t}$ tends to loosely bond to Fe1 with $r(\mathrm{Fe1{-}O3}) = 2.329$ Å. Bearing these differences in mind, one needs to be careful in comparing relative energies in the medium with different polarities.

7. Conclusions

Several models for MMOH-P peroxo intermediate, including the μ-η^2,η^2, *trans*- and *cis*-μ−1,2 $\mathrm{O_2}$ binding conformations, have been studied using broken symmetry density functional theory OPBE and PW91 functionals. By comparing the calculated geometric, energetic, and Mössbauer isomer shift and quadrupole splitting properties, model *cis*-μ−1,2a (Figure 9) is likely to represent the active site of MMOH-P as identified by Mössbauer and vibrational spectroscopies.[8] Feasible structural changes along the P → Q transformation pathway are also proposed and schematically shown in Figures 14−17. The calculated DFT activation energy from *cis*-μ−1,2a to *cis*-μ−1,2b (transient state) is about 13 kcal $\mathrm{mol^{-1}}$ below the experimental activation enthalpy $\Delta H^\ddagger = 26{-}27$ kcal $\mathrm{mol^{-1}}$. It is not clear what part of this discrepancy is the result of the structural model (omission of the extended environment, for example), and what part reflects inaccuracies in the exchange-correlation potentials used. Further experimental and theoretical studies are needed to examine these calculations. In particular, Mössbauer studies to date include protein component B, while available X-ray structures omit MMOB, so that the structural and energetic role of MMOB is still ill-defined.

Acknowledgment. We thank the NIH for financial support (GM43278 to L.N.). We thank Prof. Lawrence Que Jr. for a valuable discussion. The support of computer resources of the Scripps Research Institute is gratefully acknowledged.

Supporting Information Available: The OPBE and PW91 calculated properties in the gas phase and in the COSMO solvation model with different dielectric contants of $\epsilon = 4.0$, 10.0 (only for OPBE), and 80.0 for our four MMOH-Q models (see Figure 3 and ref 31), and all OPBE and PW91 results calculated with the dielectric contant $\epsilon = 80.0$ for MMOH-P models (PDF). This material is available free of charge via the Internet at http://pubs.acs.org.

IC701194B